Determination of stress concentration factors in offshore wind welded structures through a hybrid experimental and numerical approach

Kolios, A., Wang, L., Mehmanparast, A. & Brennan, F.

Determination of Stress Concentration Factors in Offshore Wind Welded Structures through a Hybrid Experimental and Numerical Approach

Athanasios Kolios[1], Lin Wang[2], Ali Mehmanparast[3], Feargal Brennan[1]

[1]Department of Naval Architecture, Ocean & Marine Engineering, University of Strathclyde, Glasgow, United Kingdom

[2]School of Mechanical, Aerospace and Automotive Engineering, Coventry University, Coventry, United Kingdom

[3]Offshore Energy Engineering Centre, Cranfield University, Cranfield, Bedfordshire, United Kingdom

Abstract: Offshore wind turbine (OWT) monopile support structures generally consist of steel cans connected together through circumferential welding joints. One critical factor to evaluate the localised increase in stresses is the stress concentration factor (SCF) which depends on the welding quality. The complex welding profiles in OWT monopiles makes the accurate calculation of SCF quite challenging. In this work, an innovative approach for the calculation of SCFs in offshore welded structures is proposed based on combined 3D (three-dimensional) laser scanning technology (LST) and 3D finite element analysis (FEA). The precise geometry of the welded specimens is captured using 3D LST, and then imported into a finite element software to perform 3D FEA modelling to accurately calculate SCFs. A 2D (two-dimensional) FEA model of a typical offshore welded structure with ideal geometry is also developed in this work. In addition to numerically calculate SCFs, the 2D FEA model is further combined with non-linear RSM (response surface method) to derive analytical equations, expressing SCFs of offshore welded structures in terms of key welding parameters. Both LST-FEA3D and RSM-FEA2D models are applied to calculate SCFs in large-scale S-N fatigue welded specimens. The results indicate that the LST-FEA3D approach is capable of capturing the variation of SCFs along the width of the welded specimens and identifying the critical points where fatigue crack is most likely to initiate; and the RSM-FEA2D is valuable and efficient in deriving analytical parametric equations for SCFs.

Keywords: Stress concentration factor; Offshore wind monopiles; Steel structures; Parametric equations; FEA modelling

1. Introduction

A realistic scenario from Wind Europe foresees 320 GW of wind energy capacity to be installed in the EU by 2030, with significant contribution of 66 GW from offshore wind farms (EWEA, 2015). Offshore installations benefit from higher wind speeds, unrestricted space, and lower social impact in the marine environment (Lozano-Minguez et al., 2011). Key barriers that need to be overcome towards further deployment of offshore wind farms are the high construction cost, especially foundation and electrical connection, and limitations in operation and maintenance which constitute a considerable part of life cycle costs (Ioannou et al., 2018).

The substantial wind potential in Europe has led over the last years to a considerable increase in operational wind farms, with the UK having the highest installed capacity with farms in the North Sea, Irish Sea and Baltic Sea (Kallehave et al., 2015), with plans for significant expansion in the next decade. An OWT generally comprises of a wind turbine installed on top of a structure which is resting on a foundation that is embedded in the soil transferring loads. For the efficient service life operation of these assets it is important to accurately estimate the acting loads and their resulting effects in order to evaluate their integrity and hence their residual service life. There are various types of support structures that can accommodate OWTs, while selection of the most appropriate configuration depends on a number of criteria including the water depth, the estimated environmental loads, the cost of production and installation, complexity of the design etc (Kolios et al., 2016, 2010). The monopile support structure configuration is currently adopted in most existing projects in Europe due to its simple but robust design (Gentils et al., 2017), ease of fabrication and installation. Monopiles were deemed to be economically and technically feasible for water depths of less than 30 m (Seidel, 2010); however, the limits of their applicability has shifted and monopiles have been recently deployed in water depths of around 40 m (Peeringa, 2016).

OWT monopiles are generally made of hot-rolled structural steel plates subjected to cold-rolling followed by welding in the longitudinal direction to form "cans". The individual cans are subsequently welded circumferentially to fabricate a full-length monopile (Jacob et al., 2018)(A. Mehmanparast, O. Adedipe, F. Brennan, 2016). Several types of weld joints exist, e.g. single-V butt joint, double-V butt joint, corner joint, lap joint, etc. The double-V butt joint, in which V-shape welds are on both sides of the work piece, is generally used in OWT monopiles. The state of stress of those welded joints is complex and affected by several factors, such as residual stresses and welding profiles. Welding quality can significantly affect the structural performance of OWT monopiles, as high stresses local to the welded joints could result in crack initiation and failure in monopiles. One critical factor to evaluate the stress and

66 quality of welded joints is the SCF (stress concentration factor), which is defined as the ratio
67 of the local stress at the welded region to the nominal stress. It should be noted that different
68 types of welded joints have different welding profiles and therefore the associated SCFs are
69 also different. When calculating SCFs for different welded joints, it is important to consider the
70 corresponding welding profiles.

71 Approaches used to calculate SCFs can be categorised into three groups, i.e. experimental
72 evaluations, empirical equations and FEA (Finite Element Analysis). In the experimental
73 evaluations, the local strain/stresses at the weld toe are measured with strain gauges. The
74 nominal stress can be obtained from experimental measurements or analytical calculations.
75 Experimental measurements are difficult and not always possible to put strain gauges close
76 enough to the weld toe to obtain meaningful results. Experimental methods also tend to be
77 expensive and time-consuming in cases of complicated weld profiles (Pirali, 2006). Another
78 way to obtain SCFs is to use the empirical equations, which are generally given by design
79 standards, such as API-RP2A-WSD (American Petroleum Institute, 2014) and DNVGL-ST-
80 0126 (DNV GL AS, 2016). The empirical equations are efficient in cases of simple geometries;
81 however, they are valid only for a limited range of non-dimensional geometric parameters and
82 incapable of identifying the location of the critical points where fatigue cracking is most likely
83 to initiate. An alternative way to obtain SCFs is to use FEA modelling, which is a powerful
84 method to identify the locations of critical points and is ideally suited for the calculation of SCFs
85 in complex geometries. Due to its accuracy and high fidelity, FEA has been increasingly used
86 for the calculation of SCFs in offshore welded structures (Woghiren and Brennan 2009, Hellier
87 et al 2014, Ahmadi et al., 2011a, 2011b; Lee, 1999). Considering its accuracy, the FEA
88 approach is chosen in this study to calculate SCFs in offshore welded structures.

89 Reviewing recent work related to the calculation of SCFs for offshore applications, it is found
90 that most research has taken place for tubular components and joints, and particularly for oil
91 & gas applications. More specifically, (Zhang et al., 2018) developed a novel framework for
92 deriving the unified SCFs by reducing joint modelling from multi-planar out-of-plane
93 overlapping to equivalent uniplanar non-overlapping. (Méndez et al., 2017) have performed
94 FEA simulations and fatigue behaviour evaluation through employing 3D T-welded
95 connections with intact and grinding depth conditions for A36 steel plates. (Wu and Chen,
96 2017) compared fatigue lives predicted by the fracture mechanics and S-N approaches for a
97 floating spar structure, investigating the impact of the variation of initial crack depth, critical
98 crack depth and SCFs on the ratio of the fatigue life predicted by two approaches. (Ahmadi
99 and Zavvar, 2016) investigated the effect of multi-planarity on the SCFs in offshore tubular

100　KT-joints subjected to in-plane and out-of-plane bending loads extracting results from the
101　stress analysis of FEA models, verified against available experimental data, and performing a
102　geometrically parametric investigation followed by a set of nonlinear regression analyses to
103　derive a SCF parametric equation for the fatigue analysis and design. Further, (Ahmadi, 2016)
104　derived a probability distribution model for SCFs in internally ring-stiffened tubular KT-joints of
105　offshore structures subjected to out-of-plane bending loads. In (Ahmadi et al., 2016), based
106　on results from the FEA analysis of 108 models, validated using test data obtained from the
107　experimental investigation, probability distribution models for SCFs in internally ring-stiffened
108　tubular KT-joints under four types of in-plane bending (IPB) loads were proposed.
109　(Christiansen and Tang, 2016) have employed neural networks for tubular joint optimization
110　in offshore jacket structures where influence factors (INF) and SCFs were applied to simplified
111　models of relevant tubular joints in global models in order to achieve a realistic force flow in
112　the structure. (Maheswaran and Siriwardane, 2016) have presented a comparative study of
113　the fatigue life of tubular joints in offshore jackets according to the SCFs in DNV/GL-RP-0005
114　and FEA modelling. (Yang et al., 2015) studied SCFs of negative large eccentricity tubular N-
115　joints under axial compressive loading in vertical brace through a combination of experiments
116　and FEA simulations. (Ahmadi and Lotfollahi-Yaghin, 2015) calculated SCFs due to in-plane
117　bending (IPB) loads in ring-stiffened tubular KT-joints of offshore structures through a
118　parametric study extracting data from the FEA of 118 models, which were verified using test
119　results obtained from an experimental investigation, to study the effect of geometrical
120　parameters on the weld-toe SCFs of central and outer braces in internally ring-stiffened tubular
121　KT-joints subjected to four different types of IPB loads. (Schmidt et al., 2015) performed
122　fatigue reliability analysis for brace-column connection details in a semisubmersible hull
123　applying SCFs for the selected critical hot spots, applied to the nominal component stresses
124　due to axial forces and biaxial bending and using the hot-spot stress response spectra with
125　various spectral methods to estimate fatigue damage using Miner's rule. (Lozano-Minguez et
126　al., 2014) presented a comparison between the fatigue life predictions obtained by the SCFs
127　of 3D solid FEA models considering the weldment and the existing SCF parametric equations
128　for tubular T-joints. (Ogeman et al., 2014) presented a review of different direct calculation
129　procedures to obtain the SCF based on fatigue assessment guidelines studying the
130　uncertainty in SCF computation for ship fatigue design. (Li et al., 2014) presented a numerical
131　study on girth weld of marine steel tubular piles deriving theoretically and validating the SCF
132　at pipe splice under either axial tension or in-plane bending moment. (Cao et al., 2013)
133　employed FEM methods to study the stress concentration factors of K-joints with welding
134　residual stress. (Ahmadi et al., 2013) presented results of experimental and numerical
135　investigations of the chord-side SCF distribution of central brace in internally ring-stiffened

136 tubular KT-joints. (Ahmadi and Lotfollahi-Yaghin, 2013) studied the effect of SCFs on the
137 reliability of tubular joints through constructing a database using the results of FEA carried out
138 on the right-angle two-planar tubular DKT-joints. Finally, (Chung et al., 2013) presented a
139 methodology followed in the offshore industry for the prediction of the pile fatigue induced by
140 pile hammering during installation. From this review, it can be concluded that although
141 sufficient work is present for tubular joints and FEA is often employed for parametric studies,
142 less focus has been given to simpler but thicker geometries which are particularly relevant to
143 offshore wind energy applications.

144 The FEA models used for calculating SCFs can be further categorised into two groups, i.e. 1)
145 2D (two-dimensional) FEA, in which the stress changes in the thickness direction are
146 neglected; and 2) 3D (three-dimensional) FEA, which considers the 3D geometry of
147 specimens and capable of taking account of stress changes in the thickness direction. When
148 comparing the 3D FEA, the 2D FEA is computationally efficient. In cases that welding profiles
149 remain unchanged along the thickness direction, the 2D FEA is capable of providing same
150 results as the 3D FEA. However, for a practical welded specimen, the deviation of the welding
151 profiles in the thickness direction is inevitable due to inherent complicity of welding process.
152 In order to capture the deviation of welding profiles in the thickness direction, it is necessary
153 to use 3D FEA.

154 The accuracy of 3D FEA highly depends on the accuracy of the geometry used in the 3D FEA
155 modelling, and the inaccuracies in the geometry can lead to a significant discrepancy between
156 the FEA results and experimental data. Offshore welded structures generally have complex
157 weld profiles, making the acquisition of the precise geometry of specimens used in the fatigue
158 test quite challenging. In order to obtain precise geometries containing the full characterisation
159 of weld toe profiles, it is proposed to use 3D LST (laser scanning technology) (E. Angelopoulou
160 and J. R. Wright Jr, 1999; J. Beraldin, F. Blais, 2010), which is capable of acquiring a dense
161 3D coordinate information effectively and precisely over the complex surfaces of the weld toe.

162 To the best of authors' knowledge, the combination of LST and 3D FEA for SCF calculations
163 in offshore welded structures has not been found in the literature. In this work, a LST-FEA3D
164 model, which combines 3D LST and 3D FEA, is developed for the calculation of SCFs in
165 offshore welded structures. In the LST-FEA3D model, the precise geometry of the welded
166 specimens is obtained using 3D LST, and then imported into a finite element software package
167 to perform FEA modelling to calculate SCFs. The proposed approach is applied to calculate
168 SCFs in large-scale welded specimens tested under cyclic loading to failure. The variation of
169 SCFs along the width of the welded specimens is presented and compared to identify the

170 range of SCFs in actual test specimens. Additionally, a RSM-FEA2D model, which combines
171 2D FEA with non-linear RSM (response surface method), is also developed in this work. In
172 the RSM-FEA2D model, the 2D parametric FEA model of welded specimen developed in this
173 work is used to perform a large number of 2D FEA simulations by varying the welding
174 parameters within given limits. Multivariate regression is then used to post-process the 2D
175 FEA results to establish the response surface, deriving analytical expression of SCFs in
176 offshore welded structures. The LST-FEA3D model is used for capturing actual welding profile
177 of fabricated specimens and examining detailed SCF distributions along the weld region. The
178 RSM-FEA2D model is used for deriving analytical equations to calculate SCFs. Both LST-
179 FEA3D and RSM-FEA2D models have been developed in this work for a comprehensive
180 investigation on SCF calculations of offshore welded monopile structures. The RSM-FEA2D
181 model is validated through case studies and then compared against the LST-FEA3D model.

182 This paper is structured as follows. Sections 2 and 3 present the development of the LST-
183 FEA3D and RSM-FEA2D models, respectively. Section 4 presents the validation, results and
184 discussion, followed by conclusions in Section 5.

185 **2. LST-FEA3D (Combined 3D LST and 3D FEA)**

186 A LST-FEA3D model for the calculation of SCFs in offshore welded structures is developed
187 by combining 3D LST and 3D FEA, of which details are presented below.

188 **2.1. 3D LST**

189 In order to capture the specimen geometry in full detail, a 3D scan-to-CAD system (as shown
190 in Fig. 1) is used. The 3D laser scanner is equipped with a high-resolution camera. The
191 scanning resolution used in this analysis is 0.2 mm (following a convergence study), which
192 enables the analysis to be completed with sufficiently high accuracy and at a reasonable
193 requirement of data storage. A portable scan model EXAscan[TM] and 3D data acquisition
194 software Vxelement[TM] are used to obtain the 3D scan data. A 3D scan data processing
195 platform, Geomagic Studio, is then used to create CAD models from the 3D scan data.
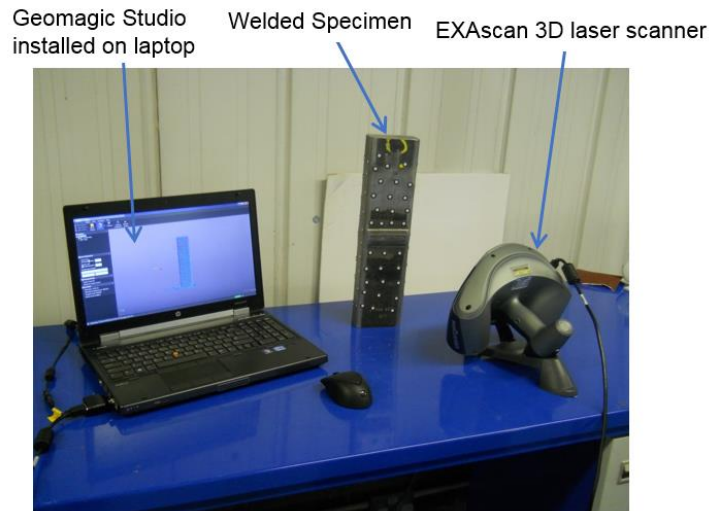
Figure 1. Setup of 3D scan-to-CAD system

The 3D laser scanning procedure comprises three main steps, i.e. pre-processing, geometry capturing and post-processing, which are detailed below:

i. Pre-processing: In this step, the specimen is cleaned prior to 3D laser scanning to remove paint/dust/grease from the surface.

ii. Geometry capturing: Having cleaned up the specimen, the scanning targets are positioned on the outer surface of the specimen, and then 3D scanning is performed by holding the trigger within the allowable range specified and moving it across the geometry.

iii. Post-processing: Once 3D scanning is completed, the captured data are post-processed by the software. The post-processing starts by reducing noise from captured data using relevant routines. The geometry alignment is then fixed with respect to the X, Y and Z coordinate axes defined in the software. Once the specimen geometry is generated by the software, the model is saved in an STL format and then converted to IGS format, which is compatible with CAD and FEA software packages. An example of the scanned geometry model is illustrated in Fig. 2.

214
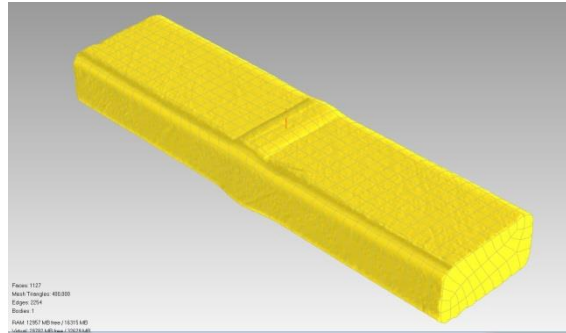
Figure 2. Scanned geometry model

2.2. 3D FEA (finite element analysis) modelling

A 3D FEA model for scanned specimens is developed using Abaqus, which is a widely used FE commercial software package. The geometry, material properties, mesh and boundary conditions used in the 3D FEA modelling are presented below.

2.2.1. Geometry

The scanned geometry is imported into Abaqus. At this stage irregular facets can be observed at both ends of the imported geometry, making it difficult to apply appropriate boundary conditions at both ends of the geometry. Cutting planes are used to trim the imported geometry, removing the irregular facets at both ends of the imported geometry and obtaining a flat plane at both ends of the geometry. The geometry after trimming is presented in Fig. 3a. At this stage a local coordinate system is defined, of which x and y axes are on the bottom plane of the specimen and the z axis is perpendicular to the bottom plane in order to reconcile between different coordinate systems across the different tools employed. The local coordinate system is depicted in Fig. 3b.


230
231   (a)   (b)
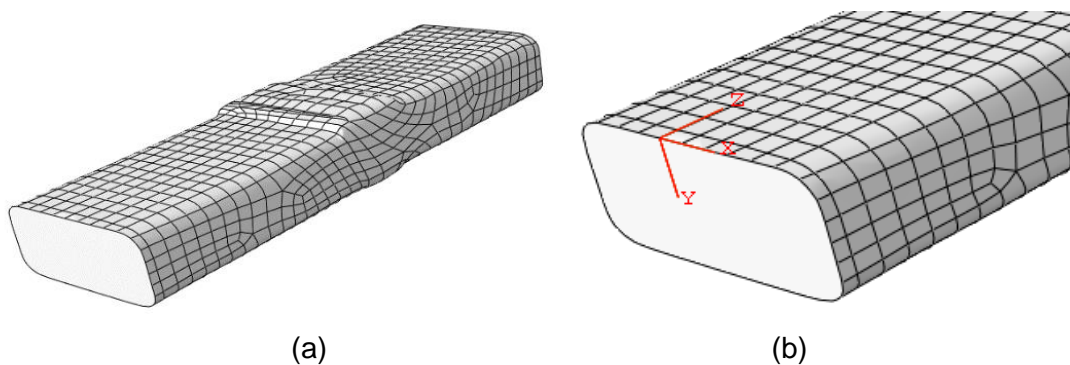
Figure 3. Geometry model: (a) geometry after trimming, (b) Local coordinate system

2.2.2. Material properties

The specimen is made of steel S355 which is a typical material used for offshore wind turbine monopiles (Igwemezie et al., 2018) with the Young's modulus of around 210 GPa and Poisson's ratio of 0.3 (Mehmanparast et al., 2018). It is worth noting that the calculated SCF values only depend on the geometry of the welded joint and are independent of the materials properties.

2.2.3. Mesh

The scanned geometry captures the details of the welding profile; however, it also makes the mesh generation quite challenging. The inherent irregular profiles of welded toes make it impossible to generate structured meshes as they cannot capture the geometrical details of interest. Therefore, unstructured mesh is used for the complicated welded geometries examined in this work. In order to determine the proper mesh size at the welding region, mesh sensitivity studies were performed. In this case, Specimen A, which was experimentally tested in this work with a load range of 875kN, is chosen as an example. Four mesh sizes at the welding regions are studied, i.e. 2 mm, 1 mm, 0.5 mm and 0.25 mm, and the mesh size of the remaining surfaces is chosen as 3.2 mm. The calculated SCFs of Specimen A are depicted in Fig. 4. As can be seen, the SCFs converge at a mesh size of 0.5 mm. Further refining mesh size to 0.25 mm does not result to significant difference in the calculated SCFs. Therefore, the mesh size of 0.5 mm is deemed as the appropriate size at the welding regions for calculating SCFs. The created mesh is depicted in Fig. 5.

253
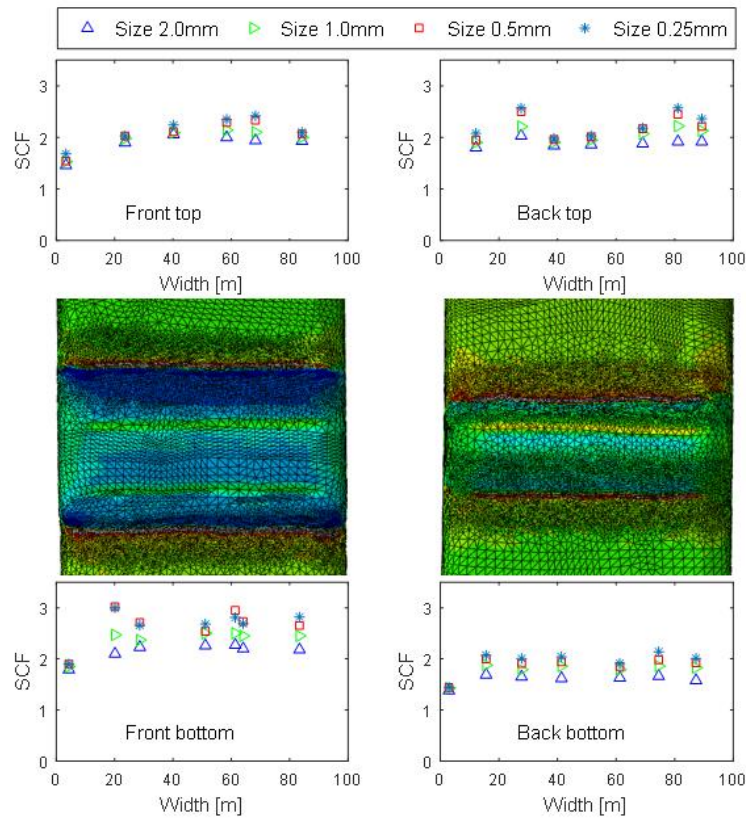
Figure 4. Mesh convergence (illustrated by results of Specimen A)
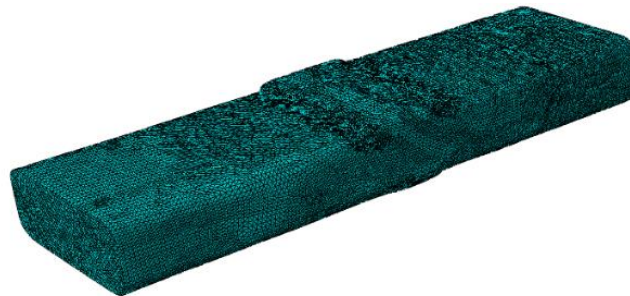
255

256   Figure 5. FEA Mesh

2.2.4. Boundary conditions

A z symmetric boundary condition, which is with respect to the created local coordinate system (see Fig. 3b in Section 2.2.1), is applied to one end of the specimen. During the experimental test in this work, specimens were tested under cyclic loading conditions with various load ranges. However, it should be noted that SCF is mainly dependent on the geometry of the welded joint, as it is the ratio of the local stress at the welded region to the nominal stress. To save computational time, instead of using cyclic loads, a uniformly distributed force with a total

264 value of 100 kN is applied to the other end of the specimen. Fig. 6 presents the boundary
265 conditions used in this study.
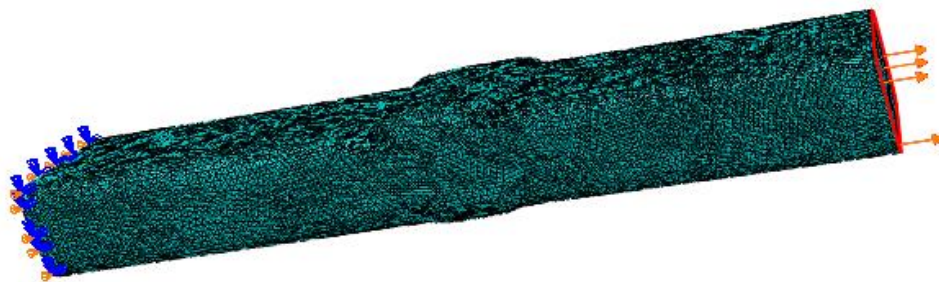
266

267 Figure 6. Boundary conditions

268 **2.2.5. FEA simulation and post-processing to derive SCFs**

269 Having defined geometry, material, mesh and boundary conditions, 3D FEA simulations were
270 performed to calculate stresses in the welded joint. In this study, a static analysis is performed.
271 After completing the simulations, the SCFs are then obtained through dividing local stresses
272 by nominal stress.

273 **2.3. Flowchart of LST-FEA3D model**

274 Fig. 7 depicts the flowchart of the LST-FEA3D model for calculating SCFs of welded
275 specimens, which combines the 3D LST (presented in Section 2.1) and the 3D FEA (presented
276 in Section 2.2).
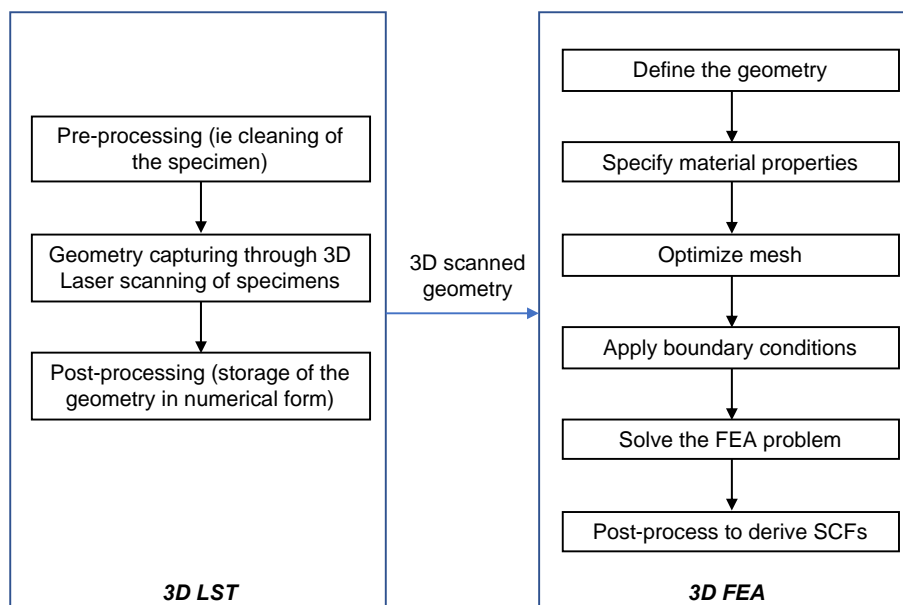
277

278   Figure 7. Flowchart of 3D LST-FEM model

279

280   3. RSM-FEA2D (Combined 2D FEA and SRM)

281   This section presents the development of the RSM-FEA2D model for the calculation of SCFs

282   in offshore welded structures, which is derived by combining 2D FEA and RSM.

283   3.1. 2D FEA modelling

284   A parametric 2D FEA model for welded specimens is developed using ANSYS, which has

285   been widely used in parametric FEA modelling. The geometry, material properties, mesh and

286   boundary conditions used in the 2D FEA model are presented below.

287   3.1.1. Geometry

288   The geometry used in the 2D FEA model is presented in Fig. 8, from which it can be seen that

289   the model includes two plates connected through the welding joint.

290

291   Figure 8. Geometry

292   3.1.2. Material properties

293   The material properties used in the 2D FEA modelling are identical to those used in 3D FEA

294   modelling (see Section 2.2.2), i.e. S355 steel having Young's modulus of 210GPa and

295   Poisson's ratio of 0.3.

296   3.1.3. Mesh

297   In this study, ANSYS adaptive mesh function is used, in which the mesh is refined

298   automatically by ANSYS until the stress results satisfy the given convergence criterion. In this

299   study, the stress variation of 1% is taken as the convergence criterion. An example of mesh

300   convergence is presented in Table 1. As can be seen from Fig. 9, the stress reaches

301   convergence at the 2nd refinement, with a relative difference of 0.09% when compared to the

302   previous solution.

303
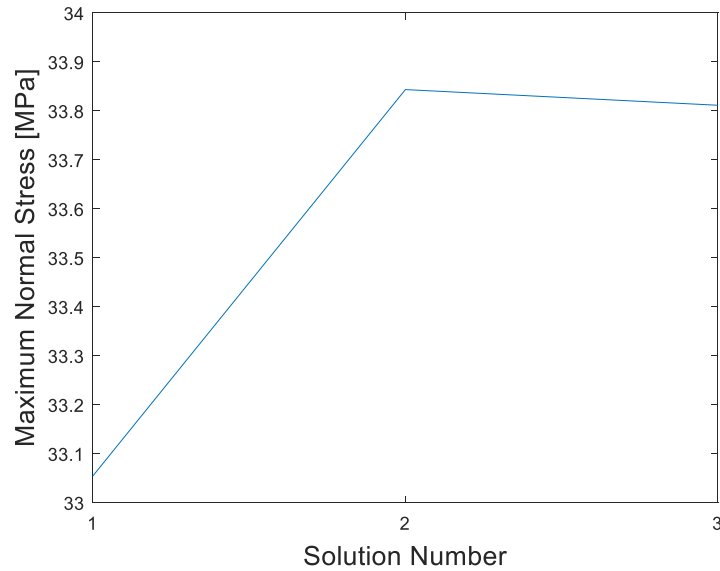
Figure 9. Mesh convergence

305

Table 1. Mesh convergence

Solution number	Maximum normal stress [MPa]	Number of elements	Relative change [%]	Mesh description
1	33.05	4,872	-	Initial mesh
2	33.84	43,234	2.39	Refinement 1
3	33.81	65,384	0.09	Refinement 2

306

3.1.4. Boundary conditions

A fixed support is applied to one end of the specimen, and a uniformly distributed force is applied to the other end. Fig. 10 depicts the boundary condition used in the 2D FEA modelling.

310

Figure 10. Boundary conditions used in 2D FEA modelling

312

3.2. Response surface method (RSM)

RSM is a comprehensive statistical approach and has been widely used to approximate the relationship between independent and dependent variable(s) (Kolios et al., 2018). It can also be considered as the function interpolating or fitting discrete data points, which determines the deterministic formulas to describe the relationship of input and output of the concerned systems based on the observed samples in the design space. The discrete data points used in the RSM can be obtained from either experiments or numerical simulations. Once the response surface (i.e. the relationship between the input and output of the concerned systems) is established, the output of the concerned system with varied input can be efficiently obtained using the established relationship. RSM therefore saves much cost and time in experiments or numerical simulations by reducing the overall number of experiments or numerical simulations required.

In this study, the discrete data points used in the RSM are obtained by performing a finite number of deterministic 2D FEA simulations using the parametric 2D FEA model presented in Section 3.1. The 2D FEA simulation results (i.e. discrete data points) are then post-processed using multivariate regression. In the general case of second-order polynomial regression without mixed terms, the problem can be described as:

$$y(x) = a_0 + a_1 x_1 + a_2 x_1^2 + a_3 x_2 + a_4 x_2^2 + \cdots + a_{2n-1} x_n + a_{2n} x_n^2 + e \qquad (1)$$

where a_i and e are the regression coefficients and the error term, respectively. Often, mixed terms are also included in the expression to account for correlated variables.

Eq. (1) can also be written in the following matrix form:

$$Y = XA + E \qquad (2)$$

where Y is a matrix containing dependent variables; X is a matrix containing independent variables; A and E are matrices with regression coefficients and error terms, respectively.

The regression coefficients A in Eq. (2) can be obtained using the LSM (Least-Square Method):

$$A = (X^T X)^{-1} XY \qquad (3)$$

338   In addition to polynomial equations, other types of equations, can also be used in RSM. A

339   such example is presented as follows.
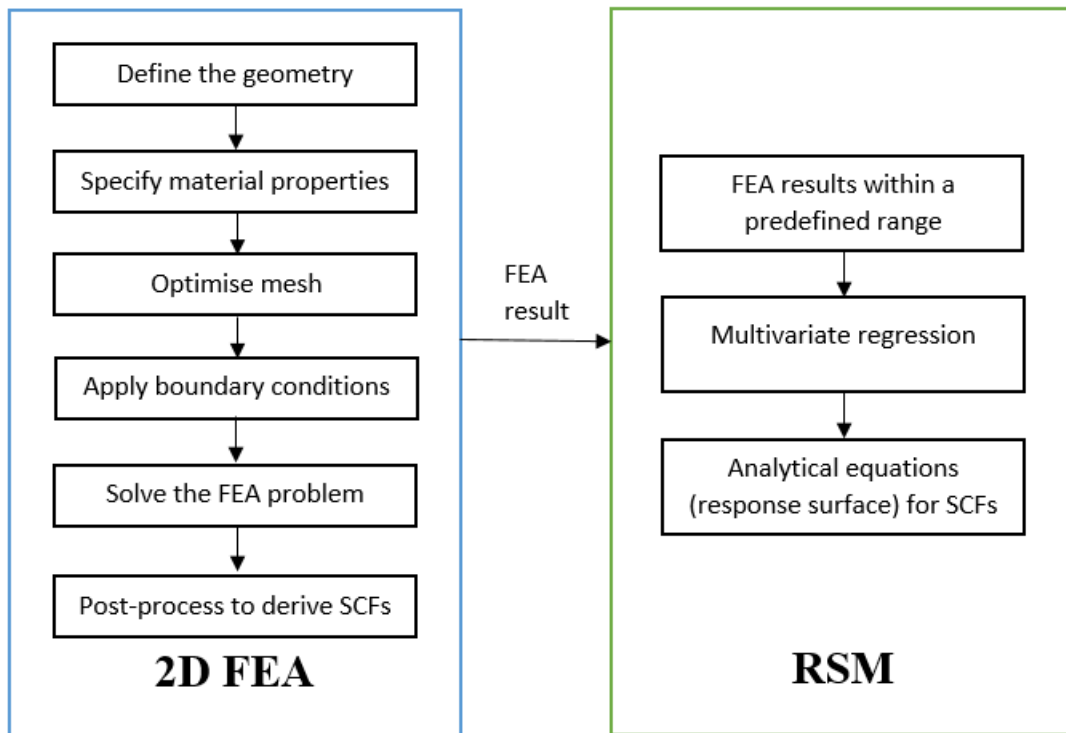
$$Y = 1 + a_0 \prod_{i=1}^{n} X_i^{a_i} \tag{4}$$

340   where a_0 and a_i are the constant coefficient and constant exponents to be fitted.

341

3.3. Flowchart of RSM-FEA2D model

343   Fig. 11 presents the flowchart of the RSM-FEA2D model for calculating SCFs, which combines

344   the 2D FEA (presented in Section 3.1) and the RSM (presented in Section 3.2).

345

346   Figure 11. Flowchart of RSM-FEA2D model for calculating SCFs

4. Results and discussion

348   The LST-FEA3D and RSM-FEA2D models for calculating SCFs of offshore wind monopile

349   structures welded specimens are developed based on the flowchart presented in Figs. 7 and

350   11, respectively. A number of case studies are performed to validate the RSM-FEA2D model.

351 After the validation, the RSM-FEA2D model is then applied to the geometries of the tested
352 specimens to derive analytical equations for calculating SCFs. The LST-FEA3D model is also
353 applied to the tested large scale specimens, obtaining detailed SCF distributions along the
354 welding regions.

355 **4.1. Testing of large scale steel specimens**

356 The specimens that were tested in this programme were in a dog-bone geometry, made of
357 S355 steel. The specimens were fabricated initially through welding of two plates (blanks) of
358 50 mm thickness with double-butt weld and then were machined into the dog-bone
359 geometries. Sharp edges were ground and shot pinned in order to avoid invalid test specimens
360 with cracks in places other than the weld region. The specimens were tested axially (tension-
361 tension) under cyclic loading conditions. Fig. 12 illustrates the experimental configuration with
362 purpose-designed mechanical grips. Before commencement of any testing, the test machine
363 Load Cell was calibrated dynamically according to relevant design standards to a level 1.5
364 times the maximum test load.

365

366 Figure 12. Experimental configuration of large scale dog-bone tests

367 **4.2. Validation of RSM-FEA2D**

368 A case study is performed to validate the RSM-FEA2D model. In this case, a plate with a hole

369 geometry (see Fig. 13) is taken as a reference geometry. The centre of the hole is located at

370 the centre of the plate, and the geometry parameters are listed in Table 2.
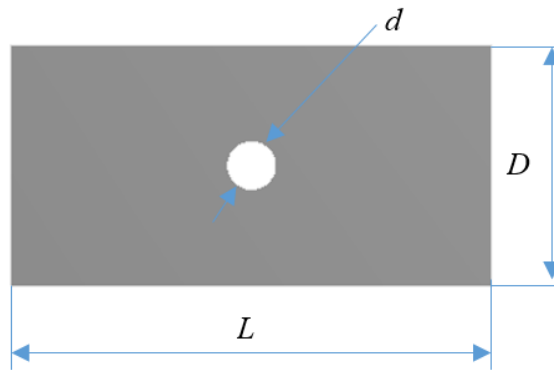
371

372 Figure 13. Geometry of plate with a hole

373 Table 2. Geometry of plate

Item	Value	Description
D [m]	5	Height
L [m]	10	Length
d [m]	$[0.1D\ 0.9D]$	Hole diameter

374

375 In this case, the left end of the plate is fixed, and the right end of the plate is loaded with a

376 force of 1MN, as illustrated in Fig. 14.

377

378 Figure 14. Boundary conditions

379   The diameter of the hole, d, is considered as a variable. 1,000 random samples are generated

380   by randomly changing the values of d within given limits of $[0.1D – 0.9D]$, i.e. $[0.5\,m – 0.45\,m]$

381   in case $D = 5\,m$. With 1,000 samples, 1,000 FEA simulations have been performed, obtaining

382   1,000 data set as illustrated in Table 3.

383   Table 3. Data set

Sample ID	d [m]	σ_{max} [Pa]	$\sigma_{nominal}$ [Pa]	$1 - d/D$ [m]	SCF
1	2.500	8,749,054	4,000,000	0.500	2.190
2	4.500	40,971,542	19,987,595	0.100	2.050
3	0.500	6,128,614	2,222,414	0.900	2.760
4	1.500	6,779,455	2,857,232	0.700	2.370
5	3.500	14,047,815	6,667,054	0.300	2.110
…	…	…	…	…	…
1000	2.380	8,403,617	3,813,760	0.520	2.200

384

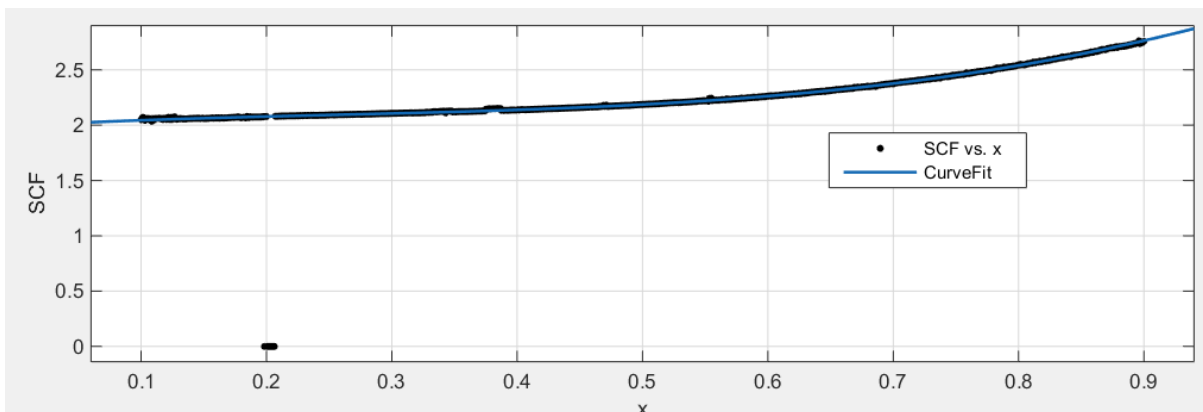385   The 1,000 FEA simulation results are then post-processed through regression, obtaining the

386   following equation for SCF:

$$SCF = 1.993 + 0.6387x - 1.431x^2 + 1.86x^3 \tag{5}$$

387   where

$$x = (1 - d/D) \tag{6}$$

388   The R^2 of the fit is 0.9927, which indicates an accurate regression. The fitted curve is shown

389   in Fig. 15.

391   Figure 15. Curve fit

392 The following expression of SCF for plate with a hole is taken from Ref. (Walter D. Pilkey,
393 2008):

$$SCF = 2 + 0.284(1 - d/D) - 0.6(1 - d/D)^2 + 1.32(1 - d/D)^3 \qquad (7)$$

394 The SCF calculated from Eq. (5), which is derived by RSM-FEA2D, is compared against the
395 SCF calculated from Eq. (7) given in Ref. (Walter D. Pilkey, 2008), as illustrated in Fig. 16. In
396 this case, the plate width D is fixed with a value of 5 m, and the hole diameter d varies between
397 0.5m and 0.45m. As can be seen from Fig. 16, the SCF obtained from the combined 2D FEA
398 and RSM show good agreement with the SCF obtained from Ref. (Walter D. Pilkey, 2008),
399 with a maximum relative difference (1.9%) observed at hole of diameter of 3.5m. This confirms
400 the validity of the RSM-FEA2D model developed in this work.
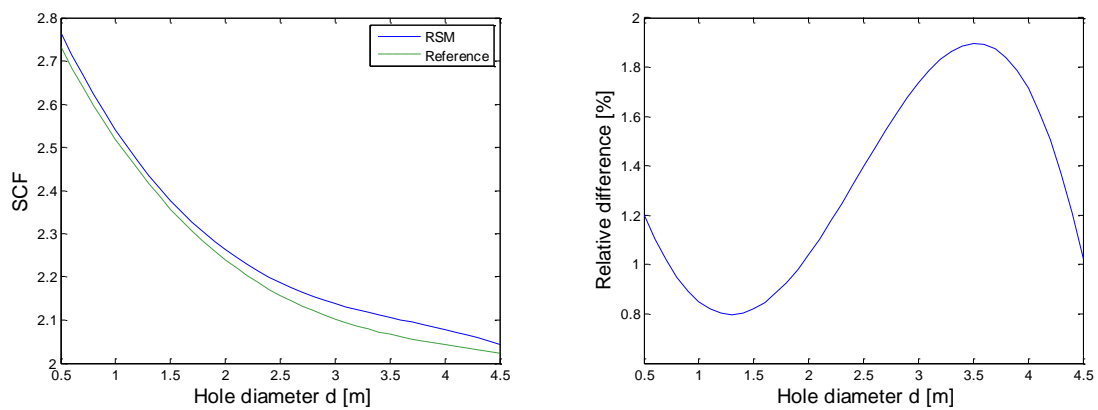
401

402 Figure 16. Calculated SCF: **a** Comparison of SCF obtained from RSM and Reference; **b**
403 Relative difference

4.3. SCF equations derived from RSM-FEA2D

405 The RSM-FEA2D model is applied to the geometries of tested specimens to derive the
406 analytical equation applicable for SCFs for offshore wind monopile welded structures. The
407 geometry of the 2D cross-section of the welded specimens used in the 2D FEA model is
408 presented in Fig. 17. As can be seen, the geometry is defined through five parameters, i.e.
409 thickness t, length L, weld height h, weld angle θ and weld toe radius r. The values of these
410 five parameters are listed in Table 4.
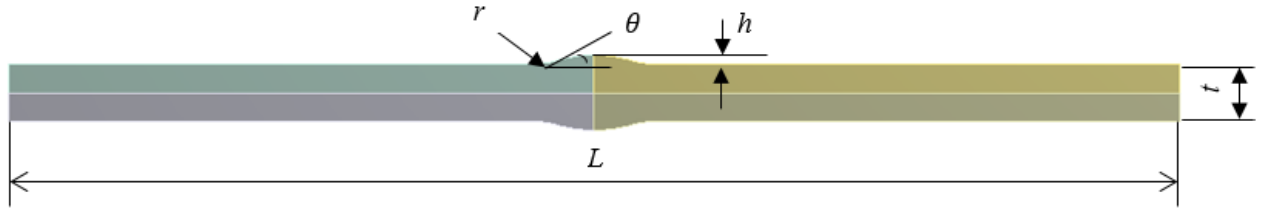
Figure 17. Geometric parameters of 2D cross-section of typical welded specimens

Table 4. Geometry parameters

Item	Value	Description
t [m]	[0.01 0.1]	Plate thickness
L [m]	1	Plate length
h/t [-]	[0.01 0.1]	Ratio of weld height h to plate thickness t
θ [deg.]	[10 45]	Weld angle
r [m]	[0.001 0.025]	Weld toe radius

All parameters in Table 4 except for plate length affect the value of SCF. Therefore, the plate length in this case is treated as constant, while the plate thickness, ratio of weld height to plate thickness h/t, weld angle θ and weld toe radius r are considered as variables. 1,000 random samples are generated by randomly changing the values of these three variables within the given limit specified in Table 4.

The 1,000 FEA simulation results are then post-processed through regression. Two forms of equations are investigated, i.e. second-order polynomial equation and multivariate power-law equation. The SCF expression derived in the form of second-order polynomial is expressed as:

$$SCF = 1.299 + 7.486\left(\frac{h}{t}\right) - 1.117\left(\frac{r}{t}\right) + 0.406\tan\theta - 34.279\left(\frac{h}{t}\right)^2 + 0.440\left(\frac{r}{t}\right)^2 \tag{8}$$
$$- 0.325(\tan\theta)^2$$

The SCF expression derived in the form of multivariate power-law equation is expressed as:

$$SCF = 1 + 0.720\left(\frac{h}{t}\right)^{0.438}\left(\frac{r}{t}\right)^{-0.458}(\tan\theta)^{0.118} \tag{9}$$

The derived SCF expression in Eq. (8) with the second-order polynomial form has a R^2 value of 0.656, which is relatively low and indicates Eq. (8) does not fit the original data well. The

427 derived SCF expression in Eq. (9) with the multivariate power-law form has a R^2 value of
428 0.970, which indicates a high accuracy regression. This indicates that the form of expression
429 used in the regression process can significantly affect the accuracy of regression. Eq. (9) has
430 high accuracy and it is therefore chosen as the analytical expression for SCF in this work.
431
432 Fig. 18 presents the comparison of the predicted data, which are obtained using Eq. (9), and
433 the original data, which are obtained from the 1,000 FEA simulations. As can be observed,
434 the predicted data show reasonable agreement with the original data. Eq. (9) derived in this
435 work can be therefore used confidently to effectively calculate the SCF of welded specimens.
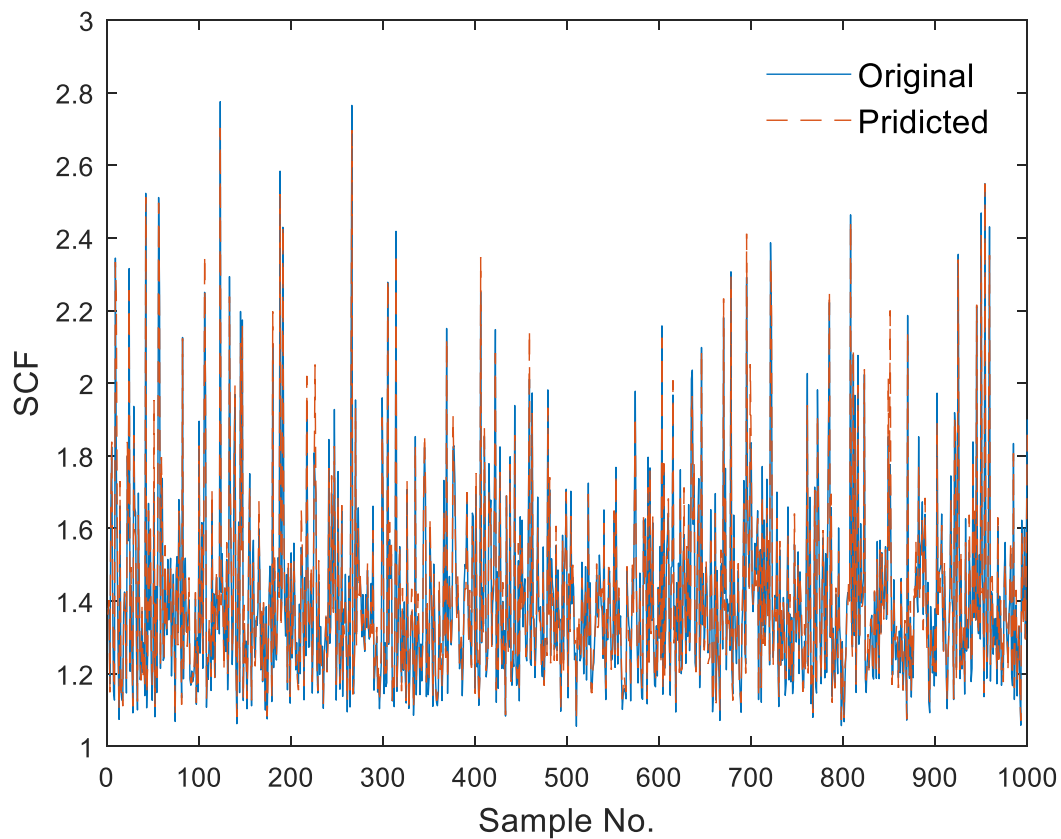
436

437 Figure 18. Comparison of original and predicted data

438 In Ref. (He and Zhang, 2011), a SCF expression for double-V butt welded joint was proposed
439 for a specific case with weld toe angle of 30°, plate thickness of 0.01m, and it is expressed as:

$$SCF = 0.817e^{-r/1.013} + 0.482e^{-r/9.717} + 0.629e^{-r/0.215} + 1.038 \qquad (10)$$

440 where r in Eq. (10) is the weld toe radius. It should be noted that r in Eq. (10) is in mm, while
441 the r in Eq. (9) is in m.

442   The SCFs calculated using Eq. (9) derived in this work are compared against the SCFs

443   calculated using Eq. (10), and the comparison results are depicted in Fig. 19. In this case,

444   weld toe angle is 30°, plate thickness is 0.01m and ratio of weld height to plate thickness is

445   0.08, and the weld toe radius varies between 0.001m and 0.008m.
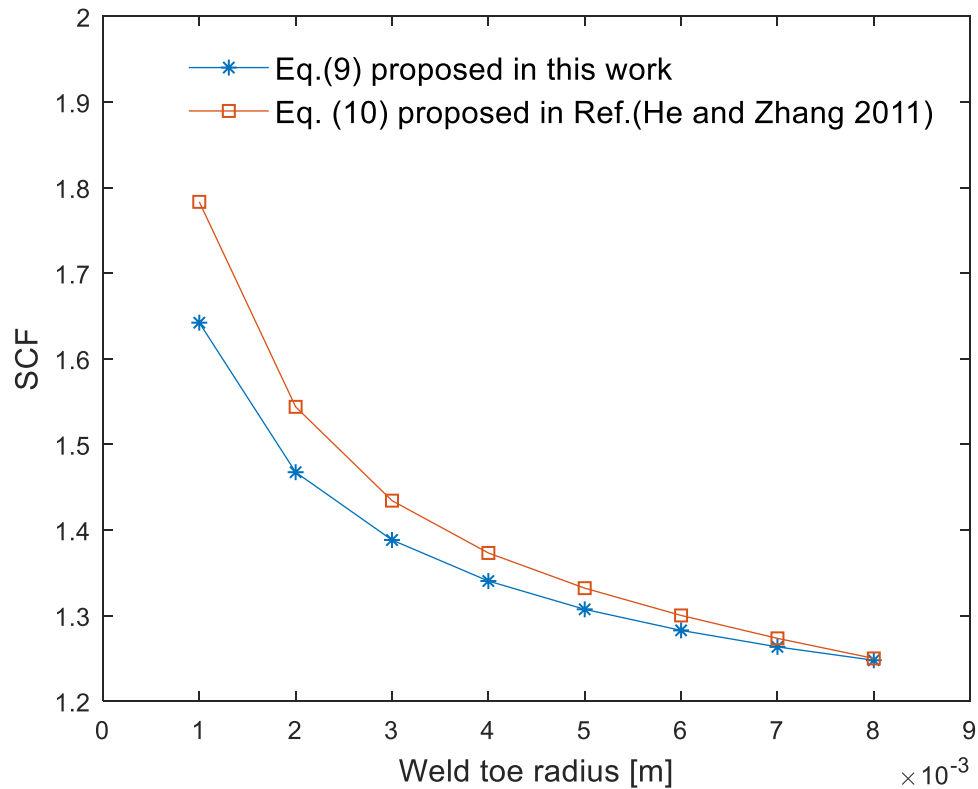
446

447   Figure 19. Calculated SCF

448   As can be seen from Fig. 19, the results from Eq. (9) derived in this work show reasonable

449   agreement with those from Eq. (10) proposed in Ref. (He and Zhang, 2011), with a maximum

450   relative difference (7.9%) observed at weld toe radius of 0.001m. This further confirms the

451   validity of the SCF equation derived in this work. Compared to Eq. (10) proposed in Ref. (He

452   and Zhang, 2011), which is limited to a single weld toe angle and plate thickness, Eq. (9)

453   derived in this work is more comprehensive as it takes account of all parameters associated

454   with SCF for double-V butt weld joints.

455

4.4. SCF distributions calculated with LST-FEA3D

The LST-FEA3D model is also applied to the geometries of the tested specimens to calculate SCFs, investigating the distribution of SCFs along the width of the welded specimens. In this work, more than 30 specimens were experimentally tested and LST-FEA3D model has been applied to all tested specimens to calculate SCFs. All specimens were manufactured based on the same technical drawing. The variations in manufactured specimens were introduced during the manufacturing process. The inherently complex welding process makes it inevitable to have some variations in actual welding profile of manufactured specimens, although all specimens were manufactured based on the same technical drawing. The manufactured specimens were experimentally tested under various load ranges. In this case, Specimens B and C, which were tested under load range of 1295kN and 1100kN respectively, are chosen as two examples. Figs. 20 and 21 present the distributions of SCFs along the welding region of Specimens B and C, respectively. From these figures it can be seen that 1) stress concentration is observed along the welding regions, as expected; 2) SCFs fluctuate significantly along the welding regions; 3) the critical point, where fatigue cracking is most likely to initiate, in Specimen B is observed at its front bottom corresponding to the peak SCF of 2.50; 4) the critical point in Specimen C is observed at front top corresponding to the peak SCF of 2.27.
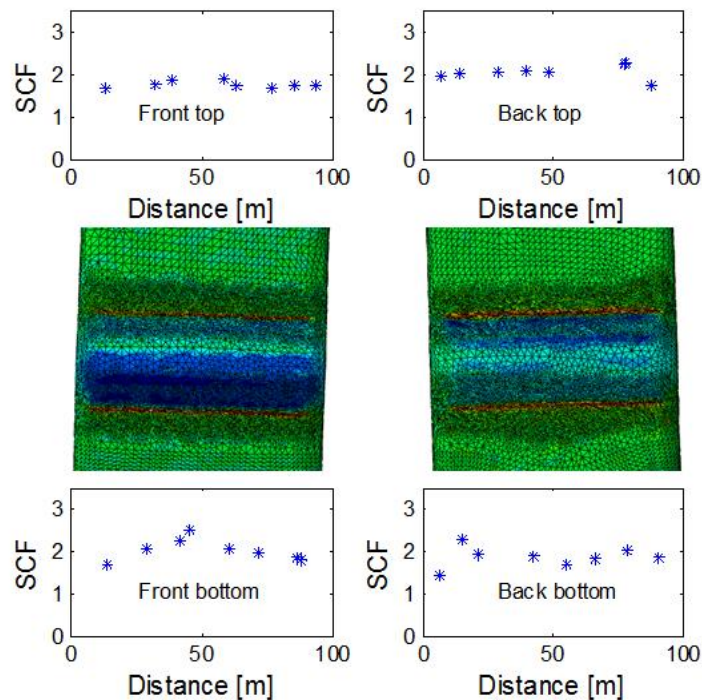
Figure 20. Distributions of SCFs of Specimen B
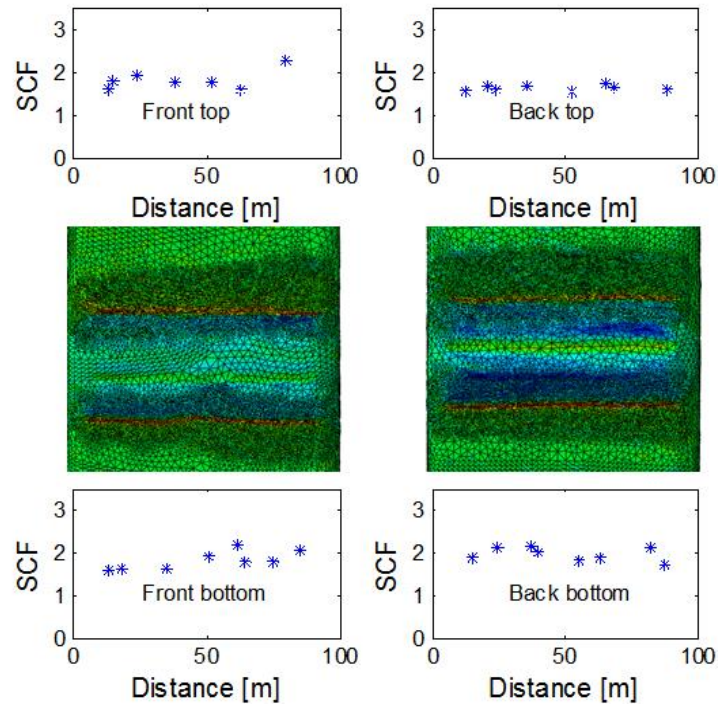
Figure 21. Distributions of SCFs of Specimen C

6. Conclusions

In this study a hybrid experimental and numerical model has been successfully developed for calculating SCFs in offshore welded structures, i.e. LST-FEA3D model and RSM-FEA2D model. The LST-FEA3D model is developed by combining the 3D (three-dimensional) LST (laser scan technology) and 3D FEA (finite element analysis). In this model, the 3D LST is used to obtain the precise geometry of the welded specimens, retaining high detail of welding profiles. The RSM-FEA2D model is developed by combining the non-linear RSM (response surface method) and the 2D FEA. In this model, a parametric 2D FEA model of butt-welded specimens is developed. A number of FEA simulations are performed by randomly varying the weld parameters within given limits. Multivariate regression is then used to post-process the FEA results, establishing the response surface. Both LST-FEA3D and RSM-FEA2D models are applied to typical offshore wind monopile welded steel specimens tested to failure under cyclic loading. The following conclusions can be drawn from the present study:

1) The analytical equation derived from the present RSM-FEA2D model, which has been validated through case studies, can efficiently calculate the SCFs of offshore welded monopile specimens.

24

2) The results from the LST-FEA3D model indicate that the SCFs along the welding region are not constant and show nonlinear distribution. This behaviour cannot be captured by conventional methods for calculating SCFs, such as empirical equations suggested by the design standards and the RSM-FEA2D model.

3) The LST-FEA3D model is demonstrated to be capable of obtaining high detail of the welding profiles and calculating SCFs along the welding regions as well as identifying the critical point where fatigue cracking is most likely to initiate.

ACKNOWLEDGEMENT

References

A. Mehmanparast, O. Adedipe, F. Brennan, and A.C., 2016. Welding sequence effects on residual stress distribution in offshore wind monopile structures. Frat. ed Integritá Strutt. https://doi.org/10.3221/IGF-ESIS.35.15

Ahmadi, H., 2016. A probability distribution model for SCFs in internally ring-stiffened tubular KT-joints of offshore structures subjected to out-of-plane bending loads. Ocean Eng. 116, 184–199. https://doi.org/10.1016/j.oceaneng.2016.02.037

Ahmadi, H., Lotfollahi-Yaghin, M.A., 2015. Stress concentration due to in-plane bending (IPB) loads in ring-stiffened tubular KT-joints of offshore structures: Parametric study and design formulation. Appl. Ocean Res. 51, 54–66. https://doi.org/10.1016/j.apor.2015.02.009

Ahmadi, H., Lotfollahi-Yaghin, M.A., 2013. Effect of SCFs on S–N based fatigue reliability of multi-planar tubular DKT-joints of offshore jacket-type structures. Ships Offshore Struct. 8, 55–72. https://doi.org/10.1080/17445302.2011.627750

Ahmadi, H., Lotfollahi-Yaghin, M.A., Aminfar, M.H., 2011a. Geometrical effect on SCF distribution in uni-planar tubular DKT-joints under axial loads. J. Constr. Steel Res. 67, 1282–1291. https://doi.org/10.1016/j.jcsr.2011.03.011

Ahmadi, H., Lotfollahi-Yaghin, M.A., Aminfar, M.H., 2011b. Effect of stress concentration factors on the structural integrity assessment of multi-planar offshore tubular DKT-joints based on the fracture mechanics fatigue reliability approach. Ocean Eng. 38, 1883–1893.

524   https://doi.org/10.1016/j.oceaneng.2011.08.004

525 Ahmadi, H., Lotfollahi-Yaghin, M.A., Yong-Bo, S., 2013. Chord-side SCF distribution of central
526   brace in internally ring-stiffened tubular KT-joints: A geometrically parametric study. Thin-
527   Walled Struct. 70, 93–105. https://doi.org/10.1016/j.tws.2013.04.011

528 Ahmadi, H., Yeganeh, A., Mohammadi, A.H., Zavvar, E., 2016. Probabilistic analysis of stress
529   concentration factors in tubular KT-joints reinforced with internal ring stiffeners under in-
530   plane bending loads. Thin-Walled Struct. 99, 58–75.
531   https://doi.org/10.1016/j.tws.2015.11.010

532 Ahmadi, H., Zavvar, E., 2016. The effect of multi-planarity on the SCFs in offshore tubular KT-
533   joints subjected to in-plane and out-of-plane bending loads. Thin-Walled Struct. 106,
534   148–165. https://doi.org/10.1016/j.tws.2016.04.020

535 American Petroleum Institute, 2014. Recommended Practice 2A-WSD for Planning,
536   Designing, and Constructing Fixed Offshore Platforms - Working Stress Design.

537 Cao, Y., Meng, Z., Zhang, S., Tian, H., 2013. FEM study on the stress concentration factors
538   of K-joints with welding residual stress. Appl. Ocean Res. 43, 195–205.
539   https://doi.org/10.1016/j.apor.2013.09.006

540 Christiansen, N.H., Tang, B.K., 2016. Neural Networks for Tubular Joint Optimization in
541   Offshore Jacket Structures, in: Volume 1: Offshore Technology; Offshore Geotechnics.
542   ASME, p. V001T01A013. https://doi.org/10.1115/OMAE2016-54846

543 Chung, J., Wallerand, R., Hélias-Brault, M., 2013. Pile Fatigue Assessment During Driving.
544   Procedia Eng. 66, 451–463. https://doi.org/10.1016/j.proeng.2013.12.098

545 DNV GL AS, 2016. DNVGL-ST-0126 Support structures for wind turbines.

546 E. Angelopoulou and J. R. Wright Jr, 1999. Laser scanner technology. Philadelphia, PA, USA.

547 EWEA, 2015. Wind energy scenarios for 2030. Brussels, Belgium.

548 Gentils, T., Wang, L., Kolios, A., 2017. Integrated structural optimisation of offshore wind
549   turbine support structures based on finite element analysis and genetic algorithm. Appl.
550   Energy 199. https://doi.org/10.1016/j.apenergy.2017.05.009

551 He, B.L., Zhang, X.D., 2011. Finite element calculation about stress concentration coefficient
552 of welded butt joints based on the ABAQUS, Applied Mechanics and Materials. Trans
553 Tech Publ, pp. 807-811.

554 Hellier, A. K., Brennan, F. P. & Carr, D. G. , 2014, Weld toe SCF and stress distribution
555 parametric equations for tension (membrane) loading, 11th International Fatigue
556 Congress. Vol. 891-892, p. 1525-1530 6 p. (Advanced Materials Research; vol. 891-
557 892)Igwemezie, V., Mehmanparast, A., Kolios, A., 2018. Materials selection for XL wind
558 turbine support structures: A corrosion-fatigue perspective. Mar. Struct. 61, 381–397.
559 https://doi.org/10.1016/j.marstruc.2018.06.008

560 Ioannou, A., Angus, A., Brennan, F., 2018. A lifecycle techno-economic model of offshore
561 wind energy for different entry and exit instances. Appl. Energy 221, 406–424.
562 https://doi.org/10.1016/j.apenergy.2018.03.143

563 Jacob, A., Oliveira, J., Mehmanparast, A., Hosseinzadeh, F., Kelleher, J., Berto, F., 2018.
564 Residual Stress Measurements in Offshore Wind Monopile Weldments using Neutron
565 Diffraction Technique and Contour Method. Theoretical and Applied Fracture Mechanics.

566 J. Beraldin, F. Blais, and U.L., 2010. Laser scanning technology, in: Airborne and Terrestrial
567 Laser Scanning.

568 Kallehave, D., Byrne, B.W., LeBlanc Thilsted, C., Mikkelsen, K.K., 2015. Optimization of
569 monopiles for offshore wind turbines. Philos. Trans. R. Soc. A Math. Phys. Eng. Sci. 373,
570 20140100–20140100. https://doi.org/10.1098/rsta.2014.0100

571 Kolios, A., Collu, M., Chahardehi, A., Brennan, F.P., Patel, M.H., 2010. A multi-criteria decision
572 making method to compare support structures for offshore wind turbines, in: European
573 Wind Energy Conference and Exhibition 2010, EWEC 2010.

574 Kolios, A., Di Maio, L.F., Wang, L., Cui, L., Sheng, Q., 2018. Reliability assessment of point-
575 absorber wave energy converters. Ocean Eng. 163, 40–50.
576 https://doi.org/10.1016/j.oceaneng.2018.05.048

577 Kolios, A., Mytilinou, V., Lozano-Minguez, E., Salonitis, K., 2016. A comparative study of
578 multiple-criteria decision-making methods under stochastic inputs. Energies 9.
579 https://doi.org/10.3390/en9070566

580 Lee, M., 1999. Estimation of stress concentrations in single-sided welds in offshore tubular

581   joints. Int. J. Fatigue 21, 895–908. https://doi.org/10.1016/S0142-1123(99)00083-3

582   Li, Y., Zhou, X.-P., Qi, Z.-M., Zhang, Y.-B., 2014. Numerical study on girth weld of marine steel
583   tubular piles. Appl. Ocean Res. 44, 112–118. https://doi.org/10.1016/j.apor.2013.11.005

584   Lozano-Minguez, E., Brennan, F.P., Kolios, A.J., 2014. Reanalysis of offshore T-joint fatigue
585   life predictions based on a complete weld profile model. Renew. Energy 71.
586   https://doi.org/10.1016/j.renene.2014.05.064

587   Lozano-Minguez, E., Kolios, A.J., Brennan, F.P., 2011. Multi-criteria assessment of offshore
588   wind turbine support structures. Renew. Energy 36.
589   https://doi.org/10.1016/j.renene.2011.04.020

590   Maheswaran, J., Siriwardane, S.C., 2016. Fatigue life estimation of tubular joints - a
591   comparative study. Fatigue Fract. Eng. Mater. Struct. 39, 30–46.
592   https://doi.org/10.1111/ffe.12314

593   Mehmanparast, A., Taylor, J., Brennan, F., Tavares, I., 2018. Experimental investigation of
594   mechanical and fracture properties of offshore wind monopile weldments: SLIC
595   interlaboratory test results. Fatigue Fract. Eng. Mater. Struct.
596   https://doi.org/10.1111/ffe.12850

597   Méndez, G.T., Cuamatzi-Meléndez, R., Hernández, A.A., Capula-Colindres, S.I., Angeles-
598   Herrera, D., Velázquez, J.C., Vazquez-Hernández, O., 2017. Correlation of Stress
599   Concentration Factors for T-Welded Connections – Finite Element Simulations and
600   Fatigue Behavior. Soldag. Inspeção 22, 194–206. https://doi.org/10.1590/0104-
601   9224/si2202.08

602   Ogeman, V., Mao, W., Ringsberg, J.W., 2014. Uncertainty in Stress Concentration Factor
603   Computation for Ship Fatigue Design, in: Volume 4A: Structures, Safety and Reliability.
604   ASME, p. V04AT02A008. https://doi.org/10.1115/OMAE2014-23129

605   Peeringa, K.H. and J., 2016. Future XL monopile foundation design for a 10 MW wind turbine
606   in deep water.

607   Pirali, M.H. and H., 2006. Hot Spot Stress Determination for a Tubular T-Joint under Combined
608   Axial and Bending Loading. IUST Int. J. Eng. Sci. 17, 21–28.

609   Schmidt, D., Manuel, L., Nguyen, H.H., Sagrilo, L.V.S., Prates de Lima, E.C., 2015. Fatigue

610   Reliability Analysis for Brace–Column Connection Details in a Semisubmersible Hull 1.
611   J. Offshore Mech. Arct. Eng. 137, 061301. https://doi.org/10.1115/1.4031493

612 Seidel, M., 2010. Feasibility of monopiles for large offshore wind turbines, in: Proceedings of
613   the 10th German Wind Energy Conference (DEWEK). REpower Systems AG. Germany.

614 Walter D. Pilkey, D.F.P., 2008. Peterson's Stress Concentration Factors, 3rd Edition.

615 Woghiren, C. O. & Brennan F. P., 2009, Weld toe stress concentrations in multi-planar
616   stiffened tubular KK joints, International Journal of Fatigue. 31, 1, p. 164-172 9 p.

617 Wu, J., Chen, N.-Z., 2017. Fracture Mechanics Based Fatigue Assessment for a Spar-Type
618   Floating Wind Turbine, in: Volume 10: Ocean Renewable Energy. ASME, p.
619   V010T09A048. https://doi.org/10.1115/OMAE2017-61568

620 Yang, J., Chen, Y., Hu, K., 2015. Stress concentration factors of negative large eccentricity
621   tubular N-joints under axial compressive loading in vertical brace. Thin-Walled Struct. 96,
622   359–371. https://doi.org/10.1016/j.tws.2015.08.027

623 Zhang, J., Jiang, J., Shen, W., Luo, Y., 2018. A novel framework for deriving the unified SCF
624   in   multi-planar   overlapped   tubular   joints.   Mar.   Struct.   60,   72–86.
625   https://doi.org/10.1016/j.marstruc.2018.03.008

626

627